Cloud-Screening Algorithm for ENVISAT/MERIS Multispectral Images

Luis Gómez-Chova, Gustavo Camps-Valls, *Senior Member, IEEE*, Javier Calpe-Maravilla, *Member, IEEE*, Luis Guanter, and José Moreno, *Associate Member, IEEE*

***Abstract*—This paper presents a methodology for cloud screening of multispectral images acquired with the Medium Resolution Imaging Spectrometer (MERIS) instrument on-board the Environmental Satellite (ENVISAT). The method yields both a discrete cloud mask and a cloud-abundance product from MERIS level-1b data on a per-pixel basis. The cloud-screening method relies on the extraction of meaningful physical features (e.g., brightness and whiteness), which are combined with atmospheric-absorption features at specific MERIS-band locations (oxygen and water–vapor absorptions) to increase the cloud-detection accuracy. All these features are inputs to an unsupervised classification algorithm; the cloud-probability output is then combined with a spectral unmixing procedure to provide a cloud-abundance product instead of binary flags. The method is conceived to be robust and applicable to a broad range of actual situations with high variability of cloud types, presence of ground covers with bright and white spectra, and changing illumination conditions or observation geometry. The presented method has been shown to outperform the MERIS level-2 cloud flag in critical cloud-screening situations, such as over ice/snow covers and around cloud borders. The proposed modular methodology constitutes a general framework that can be applied to multispectral images acquired by spaceborne sensors working in the visible and near-infrared spectral range with proper spectral information to characterize atmospheric-oxygen and water-vapor absorptions.**

***Index Terms*—Cloud screening, Medium Resolution Imaging Spectrometer (MERIS), multispectral images, spectral unmixing, unsupervised classification.**

I. Introduction

ACCURATE identification of clouds in remote-sensing images is a key issue for a wide range of remote-sensing applications, particularly in the case of sensors working in the visible and near-infrared (VNIR) range of the electromagnetic spectrum due to the severe absorption of cloud constituents. The amount of images acquired over the globe every day by the instruments on-board Earth Observation (EO) satellites makes inevitable that many of these images present cloud covers, whose extent depends on the season and the geographic position of the study region. According to the observational estimates from the International Satellite Cloud Climatology Project ISCCP-FD data set [1], the global annual-mean cloud cover is around 66%. Other studies report higher rates of cloud covers over the globe, analyzing data from a worldwide meteorological network with a large number of stations at different latitudes and seasons [2].

The presence of clouds drastically affects the measured electromagnetic signal and, thus, the retrieved information about the observed target. The corresponding cloud influence depends on the cloud type, cloud cover, cloud height, and cloud distribution in the sky, e.g., thick opaque clouds impede the incoming radiation reaching the surface, while thin transparent clouds contaminate the data by photons scattered in the observation direction, or attenuate the signal by the removal of photons in their travel to the sensor. Depending on the remote-sensing application, clouds can be either viewed as a source of contamination that makes the image partly useless for assessing landscape properties or a source of information for measuring important climatological parameters [3]. As a result, any set of remote-sensing images needs a previous cloud-screening task in the initial processing steps to ensure accuracy in the results.

Cloud-screening approaches, also referred to as cloud masking or detection, are generally based on the assumption that clouds present some useful features for its identification [4]: Clouds are usually brighter and colder than the underlying surface; clouds increase the spatial variability of detected radiance; and the spectral response is different from that of the surface covers. But, individually, each of these features in a given image is strongly conditioned by the sun elevation, variable path length, atmospheric water vapor, aerosol concentrations, variable reflectance, and subpixel clouds produced on the same pixel by cloud structures over land or sea [5]. Some of these problems can be mitigated in the cloud-screening algorithm by including specific corrections (e.g., sun elevation or path length), avoiding bands with severe atmospheric effects, and providing to the user information about subpixel coverage. The atmospheric features, although viewed as a problem by most of the cloud-screening approaches, can provide useful information about cloud height that can be included in the screening approach.

After stating the cloud-screening problem, it is clear that the selection of an approach heavily depends on the characteristics of the instrument. The spectral range, along with the spectral and spatial resolutions, is a critical factor in the selection of

Manuscript received April 30, 2007; revised June 25, 2007. This paper was supported in part by the Spanish Ministry for Education and Science under Project DATASAT (ESP2005-07724-C05-03).

L. Gómez-Chova, G. Camps-Valls, and J. Calpe-Maravilla are with the Electronics Engineering Department, University of Valencia, 46100 Valencia, Spain (e-mail: luis.gomez-chova@uv.es).

L. Guanter was with the Department of Earth Sciences and Thermodynamics, University of Valencia, 46100 Valencia Spain. He is currently with the GeoForschungsZentrum, 14473 Potsdam, Germany.

J. Moreno is with the Department of Earth Sciences and Thermodynamics, University of Valencia, 46100 Valencia, Spain.

Color versions of one or more of the figures in this paper are available online at http://ieeexplore.ieee.org.

Digital Object Identifier 10.1109/TGRS.2007.905312

the best approach. For example, the presence of channels in the thermal-infrared range enables detection based on thermal contrasts [6], [7]. Sensors with narrow spectral channels beyond 1 μm have demonstrated good capabilities to detect high clouds because of the strength of the water-vapor absorption [8], [9]. In the spectral range of 1.38–1.50 μm, both the thin cirrus clouds and the lower level cumulus clouds can be seen; however, the surface features are eliminated due to additional absorption of solar radiation by atmospheric water vapor between clouds and the surface cover (even in the presence of ice or snow). In fact, new generation EO satellites, such as GMES/Sentinel-2, include dedicated bands specifically designed to perform an accurate cloud screening. However, these features cannot be exploited by recently developed multispectral sensors that work in the spectral range between 400–1000 nm but, even in these cases, one can take advantage of their high spectral and radiometric resolution and the specific band locations to increase the cloud-detection accuracy and to properly describe detected clouds.

In this paper, we focus on the Medium Resolution Imaging Spectrometer (MERIS) instrument on-board the Environmental Satellite (ENVISAT) [10]. Two of the key features of MERIS are its temporal resolution (revisit time of three days) and its spatial coverage (swath width of 1150 km). In addition, MERIS also provides data at unprecedented spectral and spatial resolutions: 15 narrow bands and 300-m pixel size in full-resolution (FR) mode. Therefore, MERIS has a great potential for multitemporal studies, both at regional and global scales. The operational use of MERIS images is, however, hampered by the presence of clouds, because this instrument works in the VNIR part of the electromagnetic spectrum. On this matter, an automatic and accurate cloud-screening method is essential in order to use partially cloudy images facilitating the elaboration of MERIS products and also improving the usability of MERIS temporal images.

Two major points motivate the selection of MERIS data and cloud screening to be put together in this paper. On the one hand, MERIS offers a unique spectral configuration for the retrieval of both atmosphere and surface parameters: Two fine bands at the oxygen (O_2–A) and water-vapor atmospheric absorptions are combined with 13 other spectral bands providing high-accuracy measurements from the blue to the NIR spectral regions (see [10] for further technical information). In addition, the accurate characterization of the O_2–A absorption at MERIS channel 11 enables the estimation of cloud-top pressure (which is related to cloud height) from MERIS data [11]. On the other hand, there is a well-known lack of accurate methods for the cloud screening of MERIS data, as well as clearly identified problems in the corresponding European Space Agency (ESA) official level-2 (L2) cloud-mask products [12], [13].

The simplest approach to mask clouds in a particular scene is the use of a set of static thresholds (e.g., over features such as albedo or temperature) applied to every pixel in the image and ultimately providing a binary flag [14]. These methods can fail for several reasons, such as subpixel clouds, high-reflectance surfaces, illumination and observation geometry, sensor calibration, variation of the spectral response of clouds with cloud type and height, etc. [15]. Spatial-coherence methods have an advantage over static-threshold methods, because they use the local spatial structure to determine cloud-free and cloud-covered pixels. Usually, these algorithms are based on extracted textural features [16], [17], contextual approaches [7], or simple thresholds applied to the spatial variability of spectral bands [18], which is mainly applicable over the ocean, where the surface background is sufficiently homogeneous. However, spatial-coherence methods can fail when the cloud system is multilayered (which is often the case), the clouds over the scene are smaller than the instrument spatial resolution, or the scene presents cirrus clouds (which are not opaque). As a consequence, researchers have turned to developing adaptive threshold cloud-masking algorithms [15], [19], [20]. Some other algorithms take advantage of the multiangular [20], [21] or the multitemporal [22] information, depending on the instrument characteristics and the application constraints. In this context, few works using more sophisticated machine-learning tools have been presented so far, such as Bayesian methods [23], fuzzy logic [24], artificial neural networks [5], [8], [16], [25], or, recently, kernel methods [21], [26], [27]. Given the extreme complexity of cloud screening, most of the operational cloud-masking applications of current satellite multispectral systems, such as the Moderate Resolution Imaging Spectroradiometer (MODIS) [28], Along-Track Scanning Radiometer (ATSR) [15], Polarization and Directionality of the Earth's Reflectances (POLDER) [29], or MERIS [30], consist in a series of cloud-detection threshold tests, which vary depending on surface type and solar illumination.

The main objective of this paper is to develop a cloud-screening algorithm using the full spectral information provided by MERIS. The proposed cloud-screening algorithm takes advantage of the high spectral and radiometric resolutions of MERIS and the specific location of some channels (e.g., oxygen and water-vapor absorption bands) to increase the cloud-detection accuracy. The method is capable of the following: 1) detecting clouds accurately and 2) providing probability or cloud abundance rather than merely cloud flags. The cloud-abundance product provided is not directly related to the retrieval of cloud optical properties [31], such as the cloud optical thickness, which usually relies on radiative-transfer models. This added-value product allows the user to apply an adjustable cloud mask depending on the further processing stages and application of the MERIS image. For example, undetected cloudy pixels tremendously affect biophysical parameter-retrieval methods [18], [32]. Slight overmasking of potential cloudy pixels—conservative cloud masking—would be preferred in those cases in order to guarantee the quality of the final product [33], while other applications, such as land-use classification, are less sensitive to thin clouds, and thus, these areas should not be necessarily discarded [34].

The method consists of different steps. First, a feature extraction based on meaningful physical facts is carried out: clouds are bright, white, and are at a high altitude (light reflected by clouds crosses less atmosphere than the one that reaches the surface). Then, an unsupervised classification is applied to these features, and the resulting clusters are subsequently labeled as cloud or cloud-free. Finally, a spectral unmixing is applied

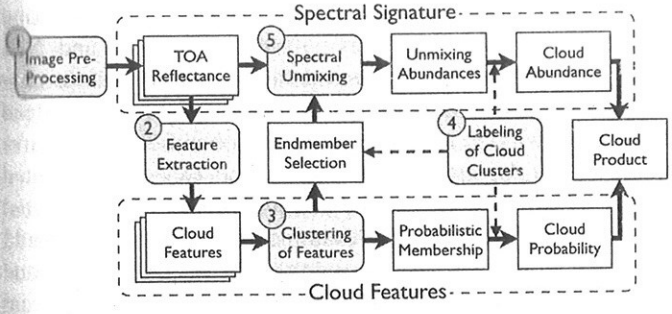

Fig. 1. Scheme of the cloud-screening algorithm constituted by the preprocessing (TOA reflectance derivation) and four main processing steps (gray boxes).

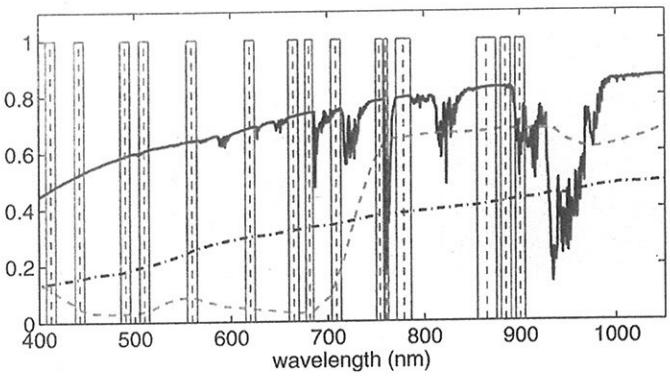

Fig. 2. (Boxes) MERIS channel locations superimposed to a reflectance spectra of (dashed) healthy vegetation, (dash-dotted) bare soil, and (solid) the atmospheric transmittance.

to the classified image. As a result, the proposed algorithm provides a per-pixel probabilistic map of cloud abundance rather than a binary cloud-presence flag.

This paper extends previous works [35], [36] as follows: 1) paying special attention to the MERIS data preprocessing; 2) analyzing the computation of atmospheric features in greater detail; 3) thoroughly testing critical situations in cloud detection (e.g., ice/snow covers); and 4) comparing results with the official L2 cloud-mask products. The rest of this paper is organized as follows. Section II describes in detail the proposed cloud-screening algorithm. In Section III, a short description of the employed MERIS images is given, and the experimental results are presented. Finally, concluding remarks and further research directions are given in Section IV.

II. Cloud-Detection Algorithm

In this section, we present a cloud-detection procedure, which is constituted by the following steps (Fig. 1).

1) Image preprocessing: A preprocessing stage of MERIS data to correct illumination effects is necessary for their proper analysis.
2) Feature extraction: Physically inspired features are extracted to increase separability of clouds and surface.
3) Image clustering: An unsupervised clustering is performed on the extracted features in order to separate clouds from the ground-cover.
4) Cluster labeling: Resulting clusters are subsequently labeled into geophysical classes according to their extracted features and spectral signatures.
5) Spectral unmixing: A spectral unmixing is applied to the segmented image in order to obtain an abundance map of the cloud content in the cloudy pixels.

In the following, we analyze these components in detail.

A. Image Preprocessing

A multispectral image acquired by a push-broom system consists of two spatial dimensions (along-track and across-track) and one spectral dimension (wavelength). The image is registered by the instrument in a data-cube where the along-track dimension y corresponds to the image lines; the across-track dimension x is associated to the pixel line; and the spectral dimension λ represents the image bands. The size of the multispectral data-cube can be written in the form $l \times p \times b$, where l is the number of image lines, p is the number of pixels per line, and b is the number of spectral channels. MERIS level-1b (L1b) products are provided in top-of-the-atmosphere (TOA) radiance (radiometrically calibrated data), and each pixel k is defined by $\{L_k(\lambda)\}_{k=1}^{n}$, where the number of pixels is $n = l \times p$ and $\mathbf{L}_k \in \mathbb{R}^b$ is the spectral signature sampled at $b = 15$ narrow bands (about 10 nm) of the VNIR spectral region $\{\lambda_i\}_{i=1}^{b} = \{412.5, 442.5, 490, 510, 560, 620, 665, 681.25, 708.75, 753.75, 760.625, 778.75, 865, 885, 900\}$ nm (see Fig. 2).

This raw information must be preprocessed in order to estimate TOA reflectance. This allows us to remove in practice the dependence on particular illumination conditions (day of the year and angular configuration) and illumination effects due to rough terrain (cosine correction), since the method is intended to work under many situations. TOA apparent reflectance is estimated according to

$$\rho(x, y, \lambda) = \frac{\pi L(x, y, \lambda)}{\cos\left(\theta(x, y)\right) F_0(\lambda)} \tag{1}$$

where $L(x, y, \lambda)$ is the provided at-sensor upward radiance at the image location (x, y), $F_0(\lambda)$ is the extraterrestrial instantaneous solar irradiance, and $\theta(x, y)$ is the angle between the illumination direction and the vector perpendicular to the surface. In this paper, $\theta(x, y)$ is computed for each pixel using the sun-azimuth and sun-zenith angles (available in the tie-point location and auxiliary data of the MERIS product) and the vector perpendicular to the surface, which can be computed from a digital elevation model (DEM). In this step, however, we assume flat surface because, by using a DEM, illumination effects in the surface are corrected but the characteristics of clouds over rough terrain may change. Finally, the sun irradiance $F_0(\lambda)$ is taken from Thuillier *et al.* [37], corrected for the acquisition day, and convolved with the MERIS spectral channels.

B. Feature Extraction

The measured spectral signature depends on the illumination, the atmosphere, and the surface. Fig. 2 shows MERIS channel locations compared with the spectral curve of healthy

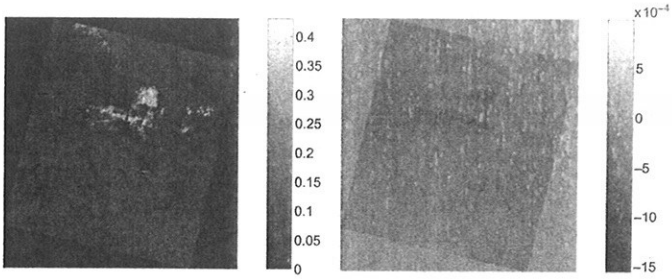

Fig. 3. (Left) Cloud brightness and (right) whiteness features extracted from the TOA reflectance of the BR-2003-07-14 image.

vegetation, bare soil, and the atmospheric transmittance. The spectral bands free from atmospheric absorptions contain information about the surface reflectance, while others are mainly affected by the atmosphere.

At this step, rather than working with the spectral reflectance only, physically inspired features are extracted in order to increase the separability of clouds and surface covers. These features are extracted independently from the channels that are free from strong gaseous absorptions ($\lambda_i \subset B_S, i = \{1\text{–}10, 12\text{–}14\}$) and from the channels substantially affected by the atmosphere ($\lambda_i \subset B_A, i = \{11, 15\}$). A detailed analysis of the extracted features follows. For illustration purposes, only the extracted features from a single given MERIS image (BR-2003-07-14, cf. Section III-A) are provided.

1) Surface Features: Regarding the reflectance of the surface, one of the main characteristics of clouds is that they present bright and white spectra (Fig. 3). We can exploit MERIS channels $\{1\text{–}10, 12\text{–}14\}$ for extracting information about the target reflectance, i.e., cloud brightness and cloud whiteness for cloudy pixels

1) A bright spectrum means that the intensity of the spectral curve (related to the albedo) should present relatively high values. Therefore, cloud brightness is calculated for each pixel as the integral of spectrum, $f_{\mathrm{Br}} = \int \rho(\lambda) d\lambda$, which is approximated through trapezoidal numerical integration

$$\hat{f}_{\mathrm{Br}} = \frac{1}{\lambda_{\max} - \lambda_{\min}} \sum_{\lambda_i \subset B_S} \frac{\rho(\lambda_{i+1}) + \rho(\lambda_i)}{2} (\lambda_{i+1} - \lambda_i) \quad (2)$$

which has the same units as $\rho(\lambda)$ and differs from the average of the spectral channels since it takes into account the distribution of the energy along the spectrum.

2) A white spectrum means that the spectral signature must be flat along the spectrum. The first derivative of the spectral curve should present low values, but noise and calibration errors may reduce the accuracy in the estimation of the spectrum flatness when computing the spectral derivative in channels with similar wavelengths. Therefore, we compute for each pixel the deviation from the flatness as the (trapezoidal approximate) integral of $e(\lambda) = |\rho(\lambda) - \hat{f}_{\mathrm{Br}}|$

$$f_{\mathrm{Wh}} = \frac{1}{\lambda_{\max} - \lambda_{\min}} \sum_{\lambda_i \subset B_S} \frac{e(\lambda_{i+1}) + e(\lambda_i)}{2} (\lambda_{i+1} - \lambda_i). \quad (3)$$

Further surface features can be obtained by considering independently the visible ($\lambda_{\mathrm{VIS}} \in [400\text{–}700]$ nm) and NIR ($\lambda_{\mathrm{NIR}} \in [700\text{–}1000]$ nm) spectral ranges, where surface covers present different reflectance properties. Therefore, instead of working with f_{Br} and f_{Wh}, we can obtain $2 + 2$ features from (2) and (3), respectively: $f_{\mathrm{Br,VIS}}$ and $f_{\mathrm{Wh,VIS}}$, computed using $\lambda_i \subset (B_S \cap \mathrm{VIS})$; and $f_{\mathrm{Br,NIR}}$ and $f_{\mathrm{Wh,NIR}}$, computed using $\lambda_i \subset (B_S \cap \mathrm{NIR})$. For example, clouds over land should be better recognized in $f_{\mathrm{Br,VIS}}$ than in $f_{\mathrm{Br,NIR}}$, since land covers have less reflectance in the VIS range, while the opposite is true for clouds over sea.

2) Atmospheric Features: Regarding the atmospheric absorptions, another meaningful feature is the fact that clouds are at a higher altitude than the surface. It is worth noting that atmospheric absorption depends on the atmospheric constituents and the optical path. Since light reflected on high clouds crosses a shorter section of the atmosphere, the consequence would be an abnormally short optical path, thus weaker atmospheric absorption features. Atmospheric-oxygen absorption and even water-vapor absorption (at 760 and 940 nm, respectively) are candidate bands to be used in the optical-path estimation.

The use of atmospheric absorption in the oxygen-A band to infer cloud pressure, which is related to cloud-top height, has been suggested by several authors [38]. In fact, cloud-top-height retrieval from the oxygen-A band using instruments conceived to yield global distributions of atmospheric constituents, such as Global Ozone Monitoring Experiment (GOME) and Scanning Imaging Absorption Spectrometer for Atmospheric Chartography (SCIAMACHY), is an active field of research [31]. In the case of medium-resolution imaging spectrometers, several studies have shown that the oxygen-A band is potentially efficient for determining the cloud-top pressure [12], [29]. All these studies assume that the two spectral channels located at the oxygen-A band (one outside and another inside the absorption) allow the derivation of an apparent pressure, which roughly represents the cloud pressure. In particular, apparent pressure is calculated using an empirical polynomial function of the oxygen transmission derived from the reflectance ratio $\rho(\lambda_{\mathrm{in}})/\rho(\lambda_{\mathrm{out}})$. However, to obtain reliable estimations of the cloud-top height is still a challenging problem affected by the instrument radiometric and spectral resolution, the influence of ground reflectance, and the need of a reliable surface-pressure reference, e.g., from the European Center for Medium-range Weather Forecasting. These difficulties explain the little attention paid to this helpful feature in cloud screening. In the case of MERIS, the accurate characterization of the O_2–A absorption at MERIS channel 11 (bandwidth of 3.75 nm nominal) makes the inclusion of this atmospheric feature in the cloud-screening scheme mandatory, as pointed in [12] and [39]. In the following paragraphs, we show the formulation proposed to extract an atmospheric feature directly related with the optical path.

The light transmitted through a nondispersive medium can be expressed using the Bouguer–Lambert–Beer law

$$L(\lambda) = L_0(\lambda) \exp\left(-\frac{\tau(\lambda)}{\mu}\right) \quad (4)$$

where $L_0(\lambda)$ is the light entering into the medium, the term $\exp(-\tau(\lambda)/\mu)$ is the transmittance factor, $1/\mu$ is the optical mass obtained from the illumination and observation zenith angles, and $\tau(\lambda)$ is the atmospheric optical depth. Since most of the radiation measured by the sensor has been reflected by the surface, (4) cannot be used to model the at-sensor radiance. However, it provides a physical basis for the definition of a nondimensional parameter that accounts for atmospheric absorptions in typical remote-sensing scenarios. In our case, the reference radiance $L_0(\lambda)$ will be the radiance outside the absorption feature, calculated by interpolating the nearby channels that are unaffected by absorptions, and $L(\lambda)$ will be the radiance affected by gaseous absorptions after crossing the TOA-surface-sensor path. The inversion of (4) provides $\tau(\lambda)$, which is a measure of the strength of the gaseous absorptions in a certain spectral range. The assumption is that variations in $\tau(\lambda)$ are driven by sharp changes in elevation as those due to transitions between cloud-free and cloud-covered areas. Horizontal variations in the atmospheric state are considered a second-order effect as compared to cloud-to-surface elevation changes. An equivalent atmospheric-transmittance parameter could be calculated as the ratio $L(\lambda)/L_0(\lambda)$, but the contribution of illumination and observation geometries would not be normalized. An additional contribution to take into account is atmospheric-path radiance, which is the radiation reflected by the atmosphere into the sensor's line-of-sight. Further refinement of (4) is achieved by removing the atmospheric-path radiance, $L_p(\lambda)$, from $L(\lambda)$ and $L_0(\lambda)$, as L_p is mainly associated to scattering processes rather than to absorption ones. In particular, L_p is calculated at each pixel using the exact pixel geometry (solar-zenith angle, viewing geometry, and surface height) from a lookup table generated with the MODTRAN4 radiative-transfer code [40]. A default visibility value of 23 km is assumed for the aerosol loading, but changes in illumination and observation angles are properly considered.

Sensor spectral calibration is a major uncertainty source when dealing with gaseous absorptions. Even though MERIS has two specific spectral bands in the oxygen-A absorption region (channels 10 and 11), the oxygen absorption is extremely narrow, and small variations of the spectral wavelength of each pixel along the charged-coupled device lines (smile effect) have a large impact on any variable derived from the oxygen-A. Fortunately, this spectral shift on the MERIS response has been well characterized, and the spectral-shift values $\Delta\lambda_i(x)$ have been provided to the user community [41]. This allows us an easy introduction of the spectral shift in our formulation.

The atmospheric optical depth is decoupled into two contributions

$$\tau(\lambda) = \tau_{\text{atm}}(\lambda) \cdot \delta \tag{5}$$

where τ_{atm} is an optical thickness reference spectrum at sea level for nadir illumination and observation, and δ is a factor accounting for elevated surfaces such as clouds. The reference $\tau_{\text{atm}}(\lambda)$ values are estimated for the channels of the instrument from a high-spectral-resolution curve. The approach followed in this paper for the so-called oxygen-A band can be devised

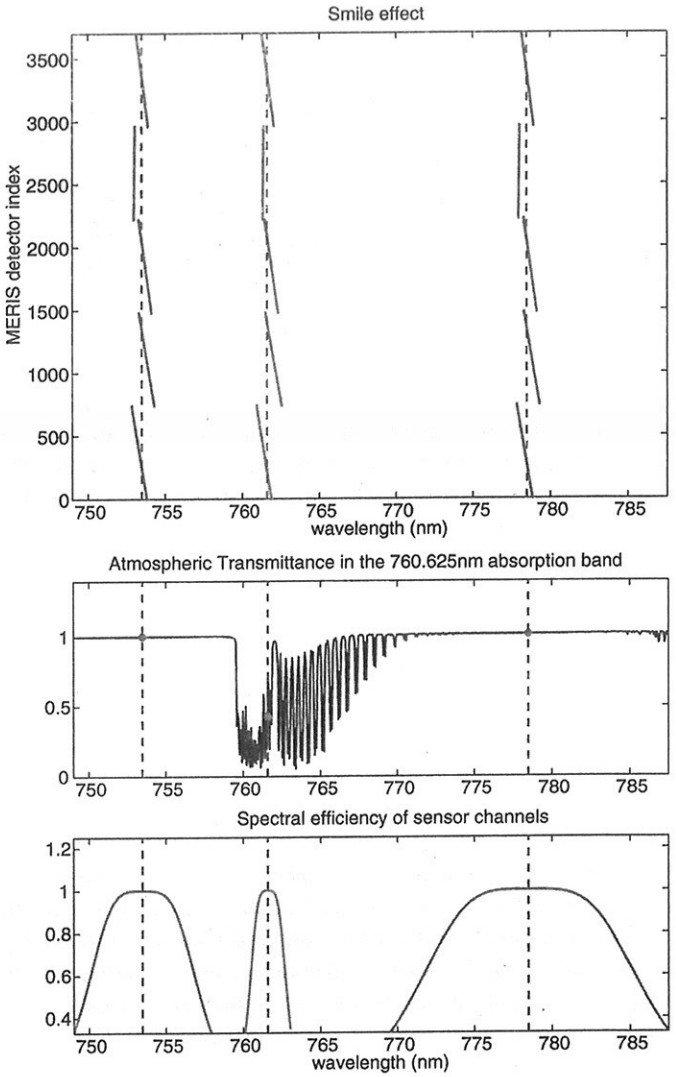

Fig. 4. Estimation of the optical path δ from the O_2 absorption band. (Top) Correction of the spectral shift on the MERIS response due to the smile effect. Figure shows the nominal wavelength λ_i of the channels $i = 10, 11, 12$ (dashed lines), and the corrected one for each MERIS detector index (constant in a given image column), $\lambda_i + \Delta\lambda_i(x)$. (Middle) Effective atmospheric vertical transmittance $\exp(-\tau_{\text{atm}}(\lambda))$ estimated from a high-resolution curve taking into account the spectral response (efficiency) of MERIS channels (Bottom).

from Fig. 4, and the extracted feature is derived from (4) and (5) as

$$f_{O_2}(x,y) = -\frac{\mu(x,y)}{\tau_{\text{atm}}\left(\lambda_{11}(x)\right)} \ln\left(\frac{L\left(x,y,\lambda_{11}(x)\right)}{L_0\left(x,y,\lambda_{11}(x)\right)}\right) \tag{6}$$

where the interpolated radiance at the absorption band is estimated from nearby channels, $L_0(\lambda_{11}) = L(\lambda_{10}) + (\lambda_{11} - \lambda_{10})(L(\lambda_{12}) - L(\lambda_{10}))/(\lambda_{12} - \lambda_{10})$, and $\tau_{\text{atm}}(\lambda)$ has been corrected for smile effect, $\lambda_i(x) = \lambda_i + \Delta\lambda_i(x)$.

An additional estimation of the optical path can be obtained from the water-vapor absorption in the NIR close to the end of the valid range of the sensor (900 nm). In this case, the maximum water-vapor absorption (940 nm) is located outside the MERIS range, and the water-vapor distribution is extremely variable, thus it is not straightforward to relate this feature to the real altitude. However, it is still valid for relative measurements

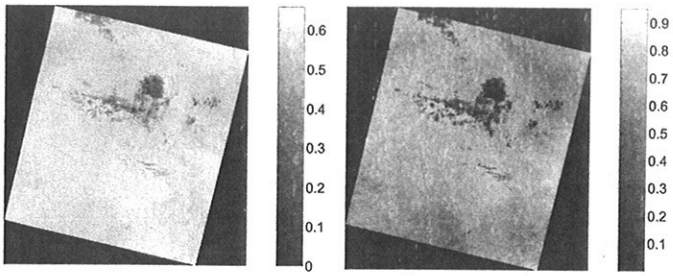

Fig. 5. (Left) Estimation of the optical path from the oxygen-absorption and (right) water-vapor bands for the BR-2003-07-14 image.

inside the same image since much of the atmospheric water vapor is distributed in the first 2–3 km of the atmosphere below most of the cloud types. Moreover, snow presents higher absorption than clouds at 900 nm, and this behavior can be appreciated in the extracted feature. The same approach as in the O_2 case has been followed to obtain this feature but using channels 14 and 15 (Fig. 5)

$$f_{\mathrm{WV}}(x,y) = -\frac{\mu(x,y)}{\tau_{\mathrm{atm}}\left(\lambda_{15}(x)\right)} \ln\left(\frac{L\left(x,y,\lambda_{15}(x)\right)}{L\left(x,y,\lambda_{14}(x)\right)}\right) \quad (7)$$

where we assume that $L_0(\lambda_{15}) = L(\lambda_{14})$ since no interpolation is possible.

It is worth noting that the extracted atmospherical features are not intended to estimate altitude of clouds. They are an estimation of the optical path by taking into account important issues such as the viewing geometry, atmospheric transmission, and sensor calibration. However, this estimation is affected by the background reflectance of the surface and the atmospheric conditions, which change from one image to another. These problems preclude the use of these features in simple approaches based on static thresholds.

As it happened with the surface features, we found differences for the retrieved-atmospheric-absorption features over land and ocean, which are mainly due to the coupling between scattering and absorption. Over dark surfaces with low reflectance, such as oceanic water, an important part of the light coming into the instrument has been scattered in the atmosphere. Therefore, the extracted features do not measure the direct oxygen or water-vapor transmittance anymore, thus resulting in a biased optical path [12], [42]. Despite of these differences over land and over ocean, the extracted features are still capable of discriminating cloud pixels in both cases for a given image. These differences on feature values over land and ocean suggest that these two different cases should be better managed separately, i.e., clustering pixels of each surface type separately.

C. Image Clustering

As previously discussed, static thresholds applied to every pixel in the image can fail due to subpixel clouds, sensor calibration, variation of the spectral response of clouds with cloud type and height, etc. In this context, the following step in our methodology considers the use of unsupervised-classification methods to find groups of similar pixels in the image. Clustering methods assume that the input data are organized into a number of groups or clusters according to a given distance measure in some representation space. We use the expectation-maximization (EM) algorithm to estimate the parameters of a Gaussian mixture model [43].

As pointed in the previous section, differences of reflectance over land and over ocean produce significant differences on the extracted features. In consequence, splitting image pixels into two different clustering problems simplifies the types of found clusters and speeds up the clustering process itself. The so-called "land/ocean" and "coastline" flags attached to the MERIS L1b product could be used to separate land and water pixels present in the image. However, this geographical product cannot be directly used for this purpose due to inaccuracies in the image geo-referentiation [44]. Therefore, a refinement process of the "land/ocean" flag is carried out on a per-pixel basis using the TOA reflectance in order to classify the inland waters and coast intertidal areas accurately. After image pixels are separated according to the surface type ("land" or "water"), the clustering is carried out. The clustering process is further described in the following sections.

1) Regions of Interest (ROIs): Before applying a clustering algorithm, we should stress the fact that, if clouds were not statistically representative in a given image, clustering methods could not find small clouds or cloud pixels could be mixed with other similar covers. Therefore, in addition to using representative features along with the spectral bands, clustering improves when applied over the regions of the image where clouds are statistically representative.

In order to find regions that could potentially contain clouds, we apply hard nonrestrictive thresholds to provide a first map of cloudlike pixels.[1] These absolute thresholds were obtained empirically and were applied to well-defined features: the brightness in the VIS and the NIR region, the estimated water-vapor absorption, and the normalized difference vegetation index (in order to exclude areas with vegetation). Then, a region-growing algorithm is carried out, along with a morphological process that dilates cloudy areas. This way, we ensure that all possible clouds and their contiguous areas will be considered in the clustering. The result of this process is far from providing a classification map but just a mask or ROI, in which the presence of clouds is significant for the purpose of clustering.

2) Clustering the ROIs: The clustering algorithm is applied to all the pixels in the ROI $\mathcal{X} = \{\mathbf{x}_k\}_{k=1}^{n}$, where $\mathbf{x}_k \in \mathbb{R}^d$ is the vector of extracted features for each pixel: $\mathbf{x}_k = \{f_{\mathrm{Br,VIS}}, f_{\mathrm{Br,NIR}}, f_{\mathrm{Wh}}, f_{\mathrm{O_2}}, f_{\mathrm{WV}}\}$. Basically, the aim of the clustering is to associate each input $\mathbf{x}_k$ to one of the clusters ω_j, $j = 1, \ldots, c$, in order to separate different classes (or at least clouds and ground-cover) present in the scene. We impose the following requirements to the clustering method: 1) taking advantage of all available features (including atmospheric absorptions); 2) considering the full relationship among variables (without applying independent tests to each feature); and 3) providing for each input soft association with the clusters

[1]Note that the MERIS L1b "bright" flag could be directly used to determine these regions to speed up the process.

(membership or probability) value between zero and one h_{kj} with the requirement that the memberships sum to one.

3) EM Algorithm: In multispectral-image processing, the assumption that the distribution of images can be approximated as a mixture of normally distributed samples is commonly accepted, and we make the same assumption for the extracted features. Therefore, we consider the input as a mixture of normal distributions and use the EM algorithm to obtain the maximum-likelihood estimation of the probability density function (pdf) of the Gaussian mixture [43]. The EM algorithm is an iterative procedure that involves two consecutive iterative steps. In the E-step, we compute the posteriors (or membership) h_{kj} of the pixel k associated to the jth Gaussian component of the mixture. In the M-step, we use the obtained h_{kj} to update the mixture coefficient α_j, the mean μ_j, and the covariance matrix Σ_j, for each component of the mixture

$$\mu_j = \frac{\sum_k h_{kj}\mathbf{x}_k}{\sum_k h_{kj}}$$

$$\Sigma_j = \frac{\sum_k h_{kj}(\mathbf{x}_k - \mu_j)(\mathbf{x}_k - \mu_j)^{\mathrm{T}}}{\sum_k h_{kj}}$$

$$\alpha_j = \frac{1}{n}\sum_k h_{kj}. \tag{8}$$

The final pdf describes both the class of interest and the ground-cover class and is worth noting that both heterogeneous classes can be made up of more than one Gaussian component, each representing a different subclass.

4) EM Initialization: The EM algorithm has to be started with initial values for the parameters of the pdf. In this paper, the k-means algorithm is used to obtain a first approach to the structure of the data in clusters. This algorithm only needs the number of clusters c to be fixed and minimizes the Euclidean distance of the samples in one cluster to its mean. In k-means, input is associated only with the cluster having the nearest center (crisp labels). The cluster center is the mean of all inputs associated with that cluster. Once the cluster centers are updated, samples may change to a different cluster so an iterative procedure is followed until centers do not change.

5) Maximum A Posteriori (MAP) Probability Classification: Once we know the Gaussian components of the pdf of the data, we perform a Gaussian maximum-likelihood classification on the whole image. The algorithm assigns the pixel to the cluster with the MAP generating a map with the clusters in the image. The final estimates of the cluster membership for each pixel in the image h_{kj} represent the estimates of the posterior probabilities, which are used to compute the optimal cluster label as

$$\hat{\omega}_k = \arg\max_j \{h_{kj}\}. \tag{9}$$

6) Remarks on the Number of Clusters: The proposed image-clustering process relies on the key step of selecting the number of clusters c. Several statistical criteria have been introduced in the literature to assess partitions produced by the EM clustering algorithm [45]. Two different indexes are used in this paper. The first one is the crisp Davies–Bouldin (DB) index [46], which consists in maximizing the between-cluster separation while minimizing the within-cluster scatter using a Euclidean metric. The second one is the minimum-description-length (MDL) criterion [47], which is an information-based probabilistic index aimed in determining the model (number of Gaussian components) that best describe the data (maximum-likelihood estimate) while reducing model complexity (number of independently adjusted parameters within the model) to account for the overfitting of high-order models.

Another possibility for the user (not explored in this paper) is to initialize the mean of the clusters with the spectral signature of the class of interest using a spectral library. Obviously, the problem of selecting c disappears if a training labeled set is available.

D. Cluster Labeling

Once clusters are determined in the previous step, the spectral signature of each cluster $\mathbf{s}_j(\lambda)$ is estimated as the average of the spectra of the cluster pixels. This step excludes those pixels with abnormally low membership values or posterior probability h_{kj}. It is important to emphasize that these spectral signatures of each cluster could differ a lot from the spectra obtained when applying the EM algorithm over the image using the spectral bands rather than the extracted features. The extracted features used to find the clusters are optimized to increase separability between clouds C and any other surface type $\overline{C}$, while in the spectral domain, these clusters could present a high degree of overlapping. Therefore, the obtained clusters can be labeled (or identified) as "cloud" or "cloud-free" (or into more detailed geophysical classes), taking into account four complementary sources of information: 1) the cluster centers μ_j of the extracted features; 2) the spectral signatures of cluster, $\mathbf{s}_j$; 3) the thematic map with the distribution of the clusters in the scene; and 4) the location in the image of the pixels with the spectral signature closer to $\mathbf{s}_j$. At this point of the process, two different labeling strategies can be followed depending on whether the method is applied to a large number of scenes in an operational mode or it is used by an operator to improve cloud screening on regional and case studies. In the first case, found clusters are labeled by using a set of threshold tests (similar to the ones used by the MERIS standard algorithm [30]) over μ_j and $\mathbf{s}_j$ values. This cluster-based approach provides a more accurate cloud screening than the standard approach (applied on a per-pixel basis) since classifying the centers of the clusters should be easier than classifying single pixels (e.g., pixels close to the decision boundaries). It is worth noting that, in this case, different classification criteria can be used for clusters found over "land" and over "water." For regional and case studies, the cluster information can be analyzed directly by the user for the given image. It can help significantly to identify clusters corresponding to extremely thin clouds or ice/snow covers misclassified by the automatic labeling. In the following processing steps of the method, both "land" and "water" clusters are used together to obtain the final probability and abundance fraction of clouds for all image pixels and, thus, obtaining a

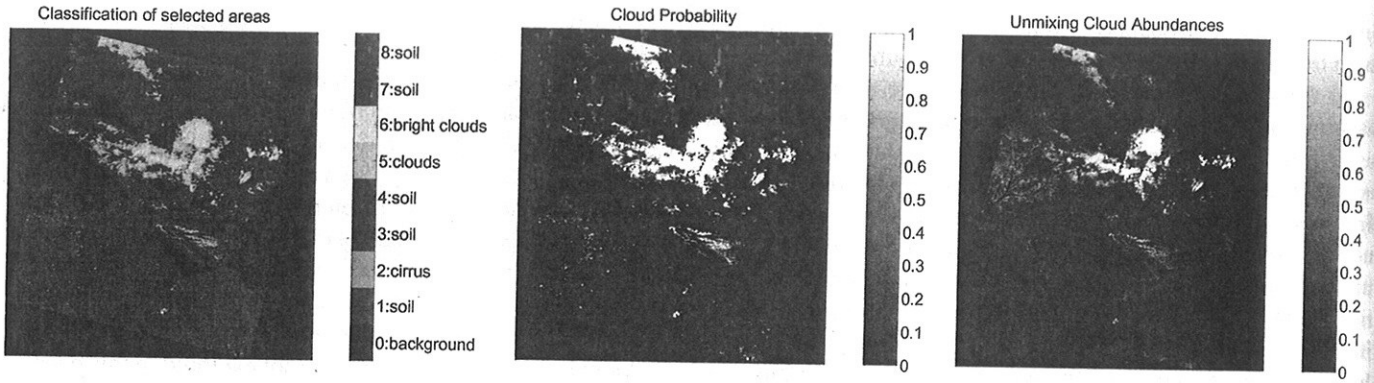

Fig. 6. (Left) Thematic map with the distribution in the scene of the classes of the clusters. (Center) Cloud-probability index computed from the posteriors of the cloud clusters. (Right) Cloud-abundance computed from the unmixing coefficients of the cloud clusters.

cloud-product map without discontinuities between land and water.

Once all clusters have been related to a class with a geophysical meaning [Fig. 6 (left)], it is straightforward to merge all the clusters belonging to a cloud type. Since the EM algorithm provides posterior probabilities ($h_{kj} \in [0,1]$ and $\sum_{j=1}^{c} h_{kj} = 1$), a probabilistic cloud index, based on the clustering of the extracted features, can be computed as the sum of the posteriors of the cloud-clusters C

$$h_{kC} = \sum_{\omega_j \subset C} h_{kj}. \tag{10}$$

However, if the clusters are well separated in the feature space, the posteriors decrease drastically from one to zero in the boundaries between clusters [Fig. 6 (center)]. Therefore, this cloud-probability index indicates the probability that one pixel belongs more to a cloud cluster C than to one of the other clusters $\overline{C}$ found in the image, but it does not give information about the cloud content at subpixel level, which is very important when dealing with thin clouds or partially covered pixels.

E. Spectral Unmixing

In order to obtain a cloud-abundance map for every pixel in the image, rather than flags or a binary classification, a spectral-unmixing algorithm is applied to the MERIS image. The linear spectral-unmixing algorithm (LSU) [48] allows decomposing each pixel of the image $\rho_k(\lambda)$ into a collection of constituent spectra or endmembers and a set of corresponding abundances that indicate the proportion of each endmember in the pixel.

1) LSU Algorithm: The algorithm used to perform the spectral unmixing is the fully constrained LSU (FCLSU) [48], which guarantees a physical interpretation of the results and can be formalized as follows:

$$\rho_k(\lambda_i) = \sum_{q=1}^{Q} m_q(\lambda_i) a_{kq} + \varepsilon_i \tag{11}$$

subject to

$$0 \le a_{kq} \le 1 \qquad \sum_{q} a_{kq} = 1 \tag{12}$$

where $\rho_k(\lambda_i)$ is the value of the pixel k for the band i, Q represents the number of endmembers that are being unmixed, being the coefficients a_{kq} of this combination the unmixing coefficients, which can be interpreted as the abundance fractions of materials in a pixel. Finally, the term ε_i represents the residual error per band. Equation (11) can be expressed in a matrix form as $\rho_k = \mathbf{M} \cdot \mathbf{a}_k + \varepsilon$, where the spectral signatures of materials $\mathbf{m}_q$ are expressed in the columns of matrix $\mathbf{M}$. The FCLSU algorithm solves a constrained linear least squares problem minimizing the norm of $(\mathbf{M} \cdot \mathbf{a}_k - \rho_k)$, where the vector $\mathbf{a}_k$ of independent variables is restricted to being nonnegative (since it represents the contribution of reflectance signatures $\mathbf{m}_q$) and sum to one (since it is supposed that $\mathbf{M}$ represents all the constituents in the image with at least one pure independent spectrum).

2) Remarks on Endmember Extraction for Cloud Screening: In the literature, there are different approaches to determine the spectra of the different pure constituents in the image [49]. However, in a cloud-screening framework, two specific considerations have to be taken into account. First, only one endmember must be selected to represent clouds. This constraint contrasts with the selection of the number of clusters, in which more clusters should model better such a heterogeneous class as clouds. In the classification, most of the cloud clusters consists of mixed pixels of thin clouds and ground or borders and subpixel clouds. In the LSU method, we assume that clouds represent pure constituents and, consequently, only one endmember must represent them. Some examples of the negative effects of including mixed thin cloud spectra as endmembers were reported in [35]. In this paper, the cloud endmember $\mathbf{m}_1$ is selected from all the cloud pixels $\rho_k \subset C$ looking for the brightest and whitest one. The second issue is related to the total number of endmembers. If the value of Q is selected to be too low, then not all constituents will be extracted. On the other hand, if the value of Q is selected to be too high, some extracted endmembers may be unwanted nonpure signatures. However, this does not constitute a critical problem since we

are not interested in obtaining accurate abundances for all the constituents present in the image but, basically, in the cloud abundance. For this reason, obtaining some unpure ground endmembers, i.e., those mixture of two or more ground constituents, is not a problem, as this will only affect the abundances related to ground endmembers.

3) Endmember-Initialization Algorithm: Taking into account the previous considerations, we use the automated target-generation process (ATGP) [50] to select the rest of endmembers $\{\mathbf{m}_q\}_{q=2}^{Q}$ from the ground pixels $\rho_k \subset \overline{C}$. The ATGP finds the endmembers in accordance with an orthogonal subspace-projection criteria, and it normally outperforms the other common endmember-initialization algorithms [49]. In particular, the ATGP is well suited to our problem since it starts with an initial endmember signature $\mathbf{m}_1$, then finds the next endmember signature $\mathbf{m}_2$ looking for the ground pixel with the maximum absolute projection in the space orthogonal to $\mathbf{M} = [\mathbf{m}_1]$, adds the new endmember to $\mathbf{M} = [\mathbf{m}_1, \mathbf{m}_2]$, and repeats the procedure until a set of Q endmembers $\{\mathbf{m}_1, \mathbf{m}_2, \ldots, \mathbf{m}_Q\}$ is extracted.

4) Cloud Abundance: After the endmember selection, we apply the FCLSU to the image using all the available spectral bands except MERIS bands particularly affected by atmospheric absorptions ($\lambda_i \subset B_A, i = \{11, 15\}$), since the linear mixing assumption is not appropriate at those bands. The FCLSU provides the vector $\mathbf{a}_k$ of abundances for each sample pixel k. As it happens with the probabilities of the clusters, the abundance $a_{kq} \in [0, 1]$ and $\sum_{q=1}^{Q} a_{kq} = 1$. Therefore, the cloud abundance is the sum of the abundances of the cloud clusters which, in our case, represents the abundance of the cloud endmember [Fig. 6 (right)]

$$a_{kC} = \sum_{q \subset C} a_{kq} = a_{k1}. \tag{13}$$

As in the case of the probabilities, a threshold of a_{kC} would give a good cloud mask but some false detections could appear since the unmixing has been performed on the basis of spectral signatures that could be nonpure pixels or, at least, not completely independent, thus providing relatively high cloud abundances in ground covers with similar spectral signatures.

5) Cloud Product: An improved cloud-product map can be obtained when combining the cloud abundance a_{kC} and the cloud probability h_{kC} by means of a pixel-by-pixel multiplication

$$\phi_k = a_{kC} h_{kC}. \tag{14}$$

That is, combining two complementary sources of information processed by independent methods: the degree of cloud abundance or mixing (obtained from the spectra) and the cloud probability that is close to one in the cloud-like pixels and close to zero in remaining areas (obtained from the extracted features). Note that, performing a pixel-by-pixel multiplication, errors in the subpixel cloud abundance would lead to similar errors in the cloud-abundance product. For example, if an endmember is selected from a ground cover with similar reflectance signature to the cloud endmember, it could introduce significant errors in the estimated cloud abundance. However, the endmember selection performed by the ATGP algorithm reduce to some extent the risk of selecting such spectra. In addition, besides abundance fractions, the unmixing algorithm provides the unmixing residual error ε, which informs us about the accuracy of the unmixing on a per-pixel basis.

III. Experimental Results

In this section, we present results of the proposed scheme. It is worth noting that validation of cloud-screening algorithms is not an easy task because there is no simultaneous independent measurement with the same spatial resolution. In this paper, we analyze the performance of the proposed method by comparing the final clustering classification and cloud-abundance product with the RGB composite of the MERIS images. In addition, a further validation step is followed by comparing results with the official MERIS L2 cloud flag.

A. Data Description

A data set consisting of four acquisitions over three sites has been selected. Both L1b and L2 products were available for all MERIS FR images (300 m). In particular, the site of Barrax (BR, Spain) was selected as the main test site. It has been the core site of previous EO campaigns, and the analyzed cloudy images are part of the data acquired in the framework of the Spectra Barrax Campaign (SPARC) 2003 and 2004 ESA campaigns (ESA-SPARC Project, Contract ESTEC-18307/04/NL/FF). These two images were acquired July 14th of two consecutive years (BR-2003-07-14 and BR-2004-07-14). Additionally, MERIS acquisitions over France (FR-2005-03-19) and Finland (FI-2005-02-26) have been included in this paper in order to take into account their different characteristics: geographic location, date and season, type of cloud, and surface types. The selected images represent different scenarios extremely useful to validate the performance of the method, including different landscapes; soils covered by vegetation or bare; and two critical cases given the special characteristics of the induced problems: ice and snow.

The proposed method is only applied to the MERIS L1b products (TOA radiance) because the top of aerosols reflectance of L2 products does not provide information at the oxygen and water-vapor absorptions. Besides, L2 products are processed from L1b using a cloud-pixel classification that could be inaccurate. Therefore, L2 products are only used for validation purposes by comparing the official L2 cloud flag with the cloud mask produced by our method.

The following results were obtained for all images and scenarios with the presented methodology as follows. The number of clusters found by the EM clustering was automatically determined as the maximum of suggested numbers by the DB and MDL indexes. However, we did not observe a critical behavior in this sense; note that even if a low number of clusters is selected, some of them should correspond to different cloud types, since the (overgrown) ROI is typically well-identified. Clusters were labeled into geo-physical classes by an operator considering the extracted features. The number of endmembers was equal to the number of clusters, and the

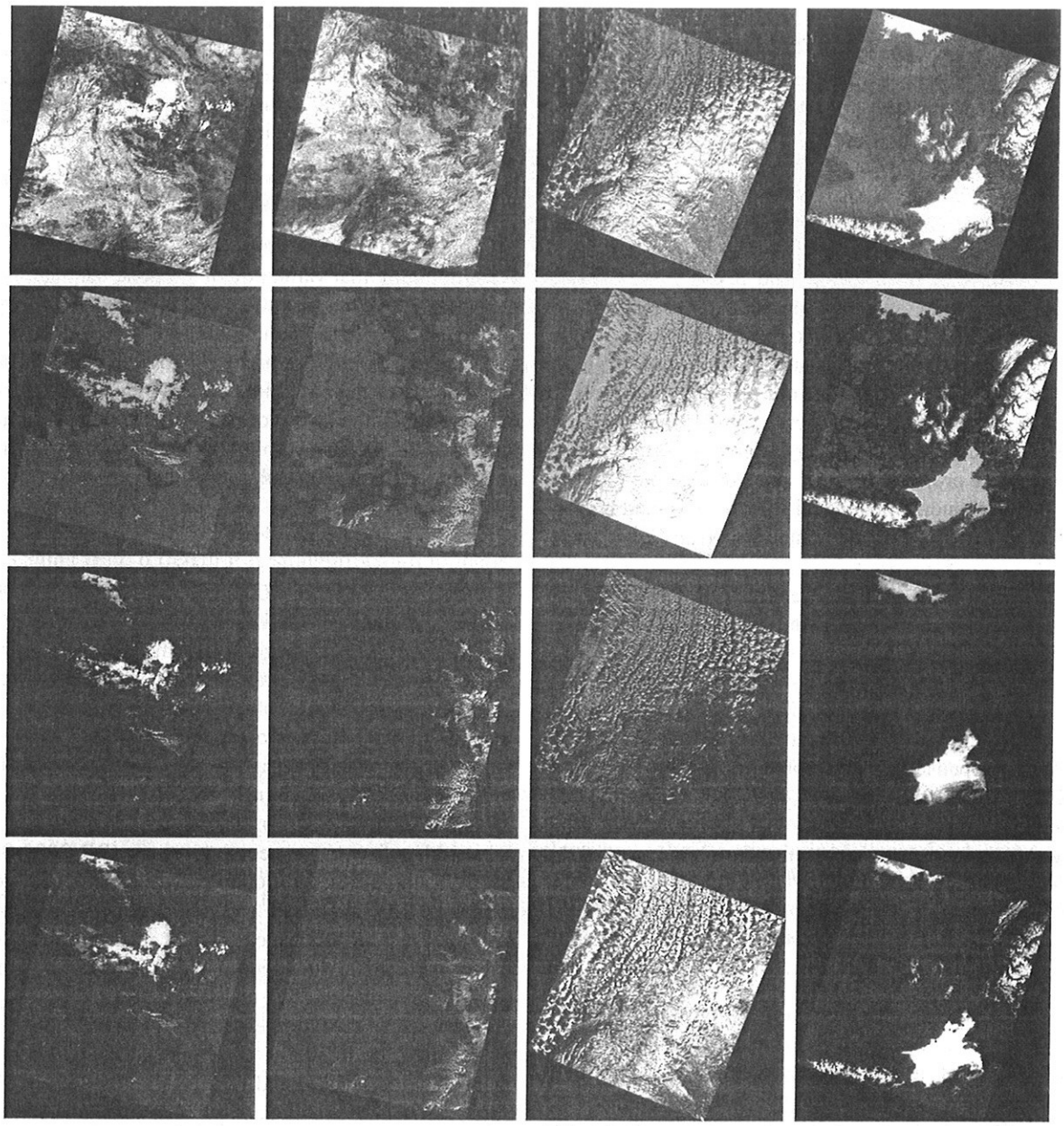

Fig. 7. MERIS images over the test sites of BR-2003-07-14, BR-2004-07-04, FI-2005-02-26, and FR-2005-03-19 displayed in columns from left to right. First row: RGB composite with a histogram stretching, such that 10% of data are saturated at both low and high reflectance (10%–90%) in order to increase the contrast of the cloudy images. Second row: Classification of the relevant regions (clouds in gray, ground in brown, ice/snow in yellow, and background in blue). Third row: Cloud-abundance product. Fourth row: Comparison of MERIS L2 Cloud Flag with the obtained cloud mask (discrepancies are shown in red when our algorithm detects cloud and in yellow when pixels are classified as cloud free).

hard classification between clouds and ground was obtained by applying a threshold of 0.05 to the cloud-abundance final product.

B. Visual Validation

1) Easy Cloud-Screening Situations: The two images over Barrax (Spain) are a good example of an easy cloud-detection problem, where opaque clouds are well contrasted with bare soil and vegetation [Fig. 7 (first and second columns)]. At the BR-2003-07-14 image, dry-soil pixels belong to a cluster labeled as cloud due to their high reflectance and whiteness, but they present low probabilities and abundances. The BR-2004-07-14 image presents thin and small clouds over land and over sea, which are well detected since a specific cluster describes them. The ROI selection can be easily seen in the classification images [Fig. 7 (second row)], being more significant in the BR-2004-07-14 image where small clouds could be mixed in a cluster with other ground covers if the whole image is considered. The use of thresholds to select the ROI could be interpreted as one of the weak points of the algorithm, since some thin or small clouds could be eventually excluded from the ROI. However, the ROI selection is an optional improvement. The obvious solution is to relax the thresholds or even consider the whole image. In this case, results are accurate if clouds cover a sufficient percentage of the image or the found

number of clusters is high enough (as in the image over Finland, FI-2005-02-26).

2) Challenging Cloud-Screening Situations: The images over Finland and France have been included in this paper to test one of the critical issues in cloud screening for which the proposed algorithm was intended for. In particular, the presented approach is designed to overcome the presence of bright pixels, such as ice and snow in the surface. Bright land covers and clouds have a similar reflectance behavior, thus thresholds on reflectance values or unmixed fractions do not solve the problem. However, the atmospheric absorption suffered by cloud pixels is lower than for the surface pixels due to their height. For this reason, when using together all the features in the clustering algorithm, different clusters are found for these two classes in the image. Owing to the extracted atmospheric features, ice/snow pixels present low cloud-probability values, although the cloud abundance provided by the spectral unmixing could be relatively high due to the spectral similarities.

Consequently, both information types are combined improving the final cloud-abundance product provided to the users [Fig. 7 (third row)]. Fig. 7 (fourth column) shows a case example result for an image over France (FR-2005-03-19) that presents opaque clouds at south and north France and snowy mountains at various altitudes (Pyrenees, Massif Central, and the Alps), which are well-distinguished from clouds. The cloud product in these regions presents low values because the low cloud probability, $h_{kC} \sim 0$, obtained for these pixels.

In the case of Finland [FI-2005-02-26, Fig. 7 (third column)], we have a different scenario where a cirrus cloud, often found in advance of a warm front, is moving from sea to the icy coast of Finland. In this image, we have a difficult cloud-identification problem, even for an expert analyst. Reflectance of transparent cirrus clouds is mostly affected by surface contribution, and it ranges from very low to extremely high values depending on whether cirrus cloud is over water or ice, respectively. However, the highest altitude clouds in the atmosphere are cirrus clouds located at altitudes between 5 and 14 km. Despite the variability of the spectral behavior, the atmospheric features allow us to cluster transparent cirrus clouds correctly. Summarizing, the use of the oxygen-A absorption allows thick and high/middle-level clouds to be detected unambiguously. Very low-level clouds, very thin cirrus clouds, and broken clouds could be undetected when using only the oxygen feature, but its combined use with surface-reflectance features solves these problems to a great extent. Finally, although the water-vapor-absorption feature is less accurate than the oxygen feature for cloud-height estimations, it provides an alternative independent estimation. Besides, it is extremely useful to discriminate clouds from ice/snow covers due to the incipient absorption of these types of covers in the NIR region above 900 nm [9].

C. Validation Against MERIS L2 Cloud Flag

One of the motivations to propose the presented cloud-screening algorithm is to solve some critical problems where the operational MERIS L2 algorithm shows clear deficiencies, as reported by the user community and by the MERIS Quality Working Group [12], [13]. For this reason, we illustrate the proposed methodology in different scenarios presenting critical cloud-screening problems and compare it to the MERIS L2 flag solution.

TABLE I
CONFUSION MATRICES BETWEEN THE PROPOSED METHOD IN THE WHOLE SCENE USING THE MERIS L2 CLOUD FLAG AS REFERENCE (GIVEN IN PERCENT OF PIXELS). IN THE BOTTOM, THE OVERALL AGREEMENT (OA%) AND ESTIMATED KAPPA STATISTICS (κ) ARE GIVEN FOR ALL IMAGES

	Proposed Method							
MERIS L2	Spain'03		Spain'04		Finland		France	
Cloud Flag	C	$\overline{C}$	C	$\overline{C}$	C	$\overline{C}$	C	$\overline{C}$
Cloud (C)	3.8	0.0	1.3	0.0	27.6	30.2	7.4	4.4
Ground ($\overline{C}$)	5.4	90.8	6.2	92.5	9.8	32.4	1.8	86.4
OA%	94.58		93.84		59.98		93.78	
$\hat{\kappa}$	0.56		0.29		0.23		0.66	

Images in the last row of Fig. 7 show a comparison of MERIS L2 Cloud Flag with the results obtained by our algorithm. Pixels where both algorithms agree are depicted in white for the cloudy pixels and in blue for the cloud-free pixels. The agreement between both methods is shown in Table I on the basis of the confusion matrices—which are expressed in terms of percentage of pixels in each image—and the overall accuracy and estimated kappa statistics[2] derived from them. Although overall agreement between both classifications is good enough for most of the images, the low values of kappa indicate that significant differences between methods exist. These differences can be better analyzed looking at the confusion matrices and comparison maps in Fig. 7. From these results, two main discrepancies can be found. On the one hand, pixels classified as cloudy pixels (C) by our method but not by the MERIS flag ($\overline{C}$) are plotted in red, showing a good agreement with cloud borders. Therefore, one can assume that the proposed method provides better recognition in cloud borders and in small and thin clouds, which is the situation in the images acquired over Spain. On the other hand, discrepancy pixels classified by our algorithm as cloud-free ($\overline{C}$) are shown in yellow. These areas correspond to ice covers (Finland image) and snow over high mountains (Pyrenees, Massif Central, and Alps in the France image). These results explain all discrepancies found in the confusion matrices and indicate the goodness of our approach.

For the sake of a fair comparison between both algorithms, we want to remark that the proposed algorithm is less efficient than the MERIS standard cloud-masking scheme in terms of computational burden (mainly due to the clustering and unmixing processes). However, when considering critical cloud-screening problems, our algorithm can provide better results. The algorithm has not been specifically designed to process a large number of images like the operational MERIS L2 algorithm or recent pragmatic solutions proposed for MERIS [39], [42]. Rather, our proposal is more concerned with obtaining abundance and accurate cloud masks when the thresholds used in the MERIS L2 algorithm are not representative.

[2]Estimated kappa statistics κ is more appropriate than the overall accuracy for testing whether agreement for both binary cloud classifiers exceeds chance levels [51]. A value of $\kappa = 1$ means complete agreement and $\kappa \leq 0$ reflects no agreement.

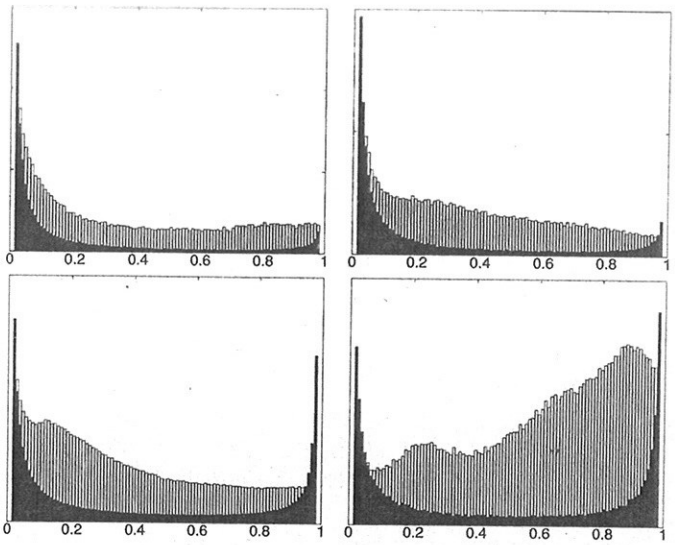

Fig. 8. Histogram of the posterior probability h_{kC} (dark) and cloud product ϕ_k (white) values for the images of BR-2003-07-14 (top left), BR-2004-07-14 (top right), FI-2005-02-26 (bottom left), and FR-2005-03-19 (bottom right). Extreme low and high values have been excluded for a proper visualization.

D. Cloud-Abundance Product

Finally, one of the requirements imposed to the proposed cloud-screening methodology was to provide information to the users about the contribution of clouds to the spectra of image pixels (for both transparent clouds or subpixel coverage situations). This type of information may be very useful for the users to decide what is a cloud depending on the application requirements or image conditions. In this paper, we classified as cloud all pixels presenting values higher than 0.05 in the obtained cloud-abundance product. It should be noted that this threshold was the same for all images analyzed in this paper. The obtained value is so low because the classification probability makes almost zero the cloud-abundance product for all the cloud-free pixels. However, if the user is not interested in excluding pixels slightly affected by clouds in a given application, threshold value can be increased.

In order to show the potential of the cloud-abundance product, Fig. 8 shows the histograms of the obtained values of posterior probability h_{kC} (dark) and cloud product ϕ_k (white) for all images. The smooth distribution of ϕ_k values differs to a great extent from the output of the probabilistic classifier, which has no physical meaning and is usually unevenly distributed around zero and one.

IV. Discussion and Conclusion

This paper presents a novel methodology that faces the challenging problem of cloud screening in ENVISAT/MERIS L1b multispectral images. The algorithm identifies the location of clouds in the image and produces a cloud-abundance map in order to quantify how cloud presence affects the measured spectra. The cloud-screening algorithm is based on well-founded physical features, which are intended to increase separability between clouds and ground covers and are extracted from the converted TOA reflectance in order to reduce dependence on illumination and geometric-acquisition conditions. Afterwards, the main modules of the cloud-screening algorithm have been formulated. An operative unsupervised classification is performed based on the extracted features in order to adapt the cloud screening to the given image conditions, mainly the atmospheric conditions, the background, and the present cloud types. This step allows the user to easily discriminate between cloud-free and cloudy regions, where the method provides a cloud-abundance product, which is based on spectral-unmixing algorithm. Method performance was validated by comparing results with the official MERIS L2 Cloud Flag and by thoroughly testing the algorithm with images representing critical situations in cloud screening.

Several remarks and conclusions can be drawn. First, the cloud-screening method has been proposed as an arrangement of different purpose-designed modules, which have been formulated in terms of simple and operational algorithms that cover the essential requirements for the cloud-screening process. These modules can be changed to more advanced algorithms or modified to adapt to the characteristics of other sensors. Consequently, this procedure can serve to develop a cloud-screening algorithm for other imaging spectrometers working in the VNIR spectral range with proper spectral characterization of the atmospheric absorptions, such as compact high resolution imaging spectrometer (CHRIS) onboard Project for On Board Autonomy (PROBA) or the future GMES/Sentinel-3 and EnMAP EO missions. The presented method was tested in a previous work [35] on PROBA/CHRIS mode-1 hyperspectral images in order to propose and validate cloud-detection methodologies. The use of CHRIS data allowed us to assess algorithm's performance in favorable spatial resolution (34 m) and number of bands (62 channels).

A second important remark is that the method has been implemented to use self-contained information provided with MERIS L1b products. It allows us to take advantage of the illumination and observation geometry and (optionally) of an overlapped DEM.

We should note that one critical feature introduced in this paper was the use of the atmospheric-oxygen and water-vapor absorption bands to improve cloud-screening results.

1) The use of atmospheric absorption in the oxygen-A band to infer cloud pressure, which is related to cloud-top height, is well-known in atmospheric studies. Here, we proposed a formulation to extract an atmospheric feature directly related with the optical path by using the exact pixel geometry.
2) Despite the high spectral and radiometric resolution of MERIS, the oxygen absorption is extremely narrow, and small variations of the spectral wavelength of each pixel have a large impact on any variable derived from the oxygen-A. In this paper, this spectral shift has been accounted for in order to correct the smile effect.
3) The maximum water-vapor absorption (940 nm) is located outside the MERIS range but absorption at 900 nm is still valid for relative measurements inside the same image. Moreover, snow presents higher absorption than clouds at 900 nm, and this behavior can be appreciated in the extracted feature.

4) Results obtained by using these absorption features suggest that it would be advantageous to see those bands included in future sensors.

An important aspect of the proposed method is that it provides a cloud-abundance product to the user that estimates the contribution of clouds to the spectra of image pixels. This information can be used to better describe detected clouds (subpixel coverage, transparency, and cloud type) and to generate cloud masks with different restrictive levels depending on the application.

Finally, results have demonstrated that the proposed algorithm accurately classifies difficult cloud pixels. In particular, clear deficiencies have been observed in the MERIS L2 Cloud Flag over bright covers, such as bare soils, ice, and snow, which are classified as clouds, and more accurate results have been obtained by the presented method in thin transparent clouds and cloud borders, which are misclassified by the official ESA product.

The presented methodology for cloud screening opens many future directions of research due to its natural modularity. Our next steps are tied to the inclusion of some refinements addressed to enhance its robustness. For instance, the inclusion of dynamic thresholds could be useful to find the regions to analyze, while the inclusion of contextual and textural information could enhance the clustering module. Some other directions will consider the inclusion of sun position to relate cloud and shadow positions.

ACKNOWLEDGMENT

The authors would like to thank ESA for the availability of the images acquired in the framework of the ESA-SPARC Project (ESTEC-18307/04/NL/FF).

REFERENCES

[1] Y. Zhang, W. B. Rossow, A. A. Lacis, V. Oinas, and M. I. Mishchenko, "Calculation of radiative fluxes from the surface to top of atmosphere based on ISCCP and other global data sets: Refinements of the radiative transfer model and the input data," *J. Geophys. Res.*, vol. 109, no. D19, D19105, 2004.

[2] F. Bréon and S. Colzy, "Cloud detection from the spaceborne POLDER instrument and validation against surface synoptic observations," *J. Appl. Meteorol.*, vol. 38, no. 6, pp. 777–785, Jun. 1999.

[3] J. P. Peixoto and A. H. Oort, *Physics of Climate*. New York: Amer. Inst. Phys., 1992.

[4] W. B. Rossow, *Clouds Atlas of Satellite Observations Related to Global Change*. Cambridge, U.K.: Cambridge Univ. Press, 1993. ch. Clouds.

[5] S. R. Yhann and J. J. Simpson, "Application of neural networks to AVHRR cloud segmentation," *IEEE Trans. Geosci. Remote Sens.*, vol. 33, no. 3, pp. 590–604, May 1995.

[6] J. J. Simpson and J. I. Gobat, "Improved cloud detection for daytime AVHRR scenes over land," *Remote Sens. Environ.*, vol. 55, no. 1, pp. 21–49, Jan. 1996.

[7] C. Papin, P. Bouthemy, and G. Rochard, "Unsupervised segmentation of low clouds from infrared METEOSAT images based on a contextual spatio-temporal labeling approach," *IEEE Trans. Geosci. Remote Sens.*, vol. 40, no. 1, pp. 104–114, Jan. 2002.

[8] T. McIntire and J. Simpson, "Arctic sea ice, cloud, water, and lead classification using neural networks and 1.6 μm data," *IEEE Trans. Geosci. Remote Sens.*, vol. 40, no. 9, pp. 1956–1972, Sep. 2002.

[9] B.-C. Gao, W. Han, S. C. Tsay, and N. F. Larsen, "Cloud detection over the arctic region using airborne imaging spectrometer data during the daytime," *J. Appl. Meteorol.*, vol. 37, no. 11, pp. 1421–1429, Nov. 1998.

[10] M. Rast and J. Bezy, "The ESA Medium Resolution Imaging Spectrometer MERIS a review of the instrument and its mission," *Int. J. Remote Sens.*, vol. 20, no. 9, pp. 1681–1702, Jun. 1999.

[11] R. Santer, V. Carrere, P. Dubuisson, and J. C. Roger, "Atmospheric correction over land for MERIS," *Int. J. Remote Sens.*, vol. 20, no. 9, pp. 1819–1840, Jun. 1999.

[12] D. Ramon, L. Cazier, and R. Santer, "The surface pressure retrieval in the MERIS O_2 absorption: Validation and potential improvements," in *Proc. IGARSS*, Toulouse, France, Jul. 2003, vol. 5, pp. 3126–3128.

[13] The MERIS Quality Working Group, *MERIS Products Quality Status Report (MEGS7.4 and IPF 5)*, Mar. 2006, Paris, France: Eur. Space Agency. Tech. Rep. issue 1. [Online]. Available: http://earth.esa.int/pcs/envisat/meris/documentation/

[14] M. Wang and W. Shi, "Cloud masking for ocean color data processing in the coastal regions," *IEEE Trans. Geosci. Remote Sens.*, vol. 44, no. 11, pp. 3105–3196, Nov. 2006.

[15] J. Simpson, A. Schmidt, and A. Harris, "Improved cloud detection in Along Track Scanning Radiometer (ATSR) data over the ocean," *Remote Sens. Environ.*, vol. 65, no. 1, pp. 1–24, Jul. 1998.

[16] B. Tian, M. Shaikh, M. Azimi, T. Haar, and D. Reinke, "A study of cloud classification with neural networks using spectral and textural features," *IEEE Trans. Neural Netw.*, vol. 10, no. 1, pp. 138–151, Jan. 1999.

[17] C. I. Christodoulou, S. C. Michaelides, and C. S. Pattichis, "Multifeature texture analysis for the classification of clouds in satellite imagery," *IEEE Trans. Geosci. Remote Sens.*, vol. 41, no. 11, pp. 2662–2668, Nov. 2003.

[18] J. Martins, D. Tanré, Y. Remer, L. Kaufman, S. Mattoo, and R. Levy, "MODIS cloud screening for remote sensing of aerosols over oceans using spatial variability," *Geophys. Res. Lett.*, vol. 29, no. 12, 8009, Jun. 2002.

[19] A. Di Vittorio and W. Emery, "An automated, dynamic threshold cloud-masking algorithm for daytime AVHRR images over land," *IEEE Trans. Geosci. Remote Sens.*, vol. 40, no. 8, pp. 1682–1694, Aug. 2002.

[20] Y. Yang, L. Di Girolamo, and D. Mazzoni, "Selection of the automated thresholding algorithm for the Multi-angle Imaging SpectroRadiometer radiometric camera-by-camera cloud mask over land," *Remote Sens. Environ.*, vol. 107, no. 1/2, pp. 159–171, Mar. 2007.

[21] D. Mazzoni, M. Garay, R. Davies, and D. Nelson, "An operational MISR pixel classifier using support vector machines," *Remote Sens. Environ.*, vol. 107, no. 1/2, pp. 149–158, Mar. 2007.

[22] K. Saitwal, M. Azimi-Sadjadi, and D. Reinke, "A multichannel temporally adaptive system for continuous cloud classification from satellite imagery," *IEEE Trans. Geosci. Remote Sens.*, vol. 41, no. 5, pt. 2, pp. 1098–1104, May 2003.

[23] F. Murtagh, D. Barreto, and J. Marcello, "Decision boundaries using Bayes factors: The case of cloud masks," *IEEE Trans. Geosci. Remote Sens.*, vol. 41, no. 12, pp. 2952–2958, Dec. 2003.

[24] A. Ghosh, N. Pal, and J. Das, "A fuzzy rule based approach to cloud cover estimation," *Remote Sens. Environ.*, vol. 100, no. 4, pp. 531–549, Feb. 2006.

[25] J. A. T. Arriaza, F. G. Rojas, M. P. López, and M. Cantón, "An automatic cloud-masking system using backpro neural nets for AVHRR scenes," *IEEE Trans. Geosci. Remote Sens.*, vol. 41, no. 4, pp. 826–831, Apr. 2003.

[26] Y. Lee, G. Wahba, and S. Ackerman, "Cloud classification of satellite radiance data by multicategory support vector machines," *J. Atmos. Ocean. Technol.*, vol. 21, no. 2, pp. 159–169, Feb. 2004.

[27] L. Gómez-Chova, G. Camps-Valls, J. Muñoz-Marí, and J. Calpe-Maravilla, "Semi-supervised cloud screening with Laplacian SVM," in *Proc. IGARSS*, Barcelona, Spain, Jul. 2007.

[28] S. Ackerman, K. Strabala, W. Menzel, R. Frey, C. Moeller, and L. Gumley, "Discriminating clear sky from clouds with MODIS," *J. Geophys. Res.*, vol. 103, no. D24, pp. 32 141–32 157, 1998.

[29] J. C. Buriez, C. Vanbauce, F. Parol, P. Goloub, M. Herman, B. Bonnel, Y. Fouquart, P. Couvert, and G. Seze, "Cloud detection and derivation of cloud properties from POLDER," *Int. J. Remote Sens.*, vol. 18, no. 13, pp. 2785–2813, Sep. 1997.

[30] R. Santer, V. Carrère, D. Dessailly, P. Dubuisson, and J. Rogerin "MERIS algorithm theoretical basis document (ATBD 2.17). Pixel identification," Eur. Space Agency, Paris, France, Dec. 1997. Tech. Rep. issue 4. [Online]. Available: http://envisat.esa.int/instruments/meris/atbd

[31] A. Kokhanovsky, T. Nauss, M. Schreier, W. von Hoyningen-Huene, and J. Burrows, "The intercomparison of cloud parameters derived using multiple satellite instruments," *IEEE Trans. Geosci. Remote Sens.*, vol. 45, no. 1, pp. 195–200, Jan. 2007.

[32] Y. Kaufman, L. Remer, and D. Tanré, "A critical examination of the residual cloud contamination and diurnal sampling effects on MODIS estimates of aerosol over ocean," *IEEE Trans. Geosci. Remote Sens.*, vol. 43, no. 12, pp. 2886–2897, Dec. 2005.

[33] L. Guanter, M. C. González-Sampedro, and J. Moreno, "A method for the atmospheric correction of ENVISAT/MERIS data over land targets," *Int. J. Remote Sens.*, vol. 28, no. 3/4, pp. 709–728, Jan. 2007.

[34] L. Gómez-Chova, R. Zurita-Milla, G. Camps-Valls, L. Guanter, J. Clevers, J. Calpe, M. Schaepman, and J. Moreno, "Cloud screening and multitemporal unmixing of MERIS FR data," in *Proc. ENVISAT Symp.*, Apr. 2007.
[35] L. Gómez-Chova, J. Amorós, G. Camps-Valls, J. Martín, J. Calpe, L. Alonso, L. Guanter, J. Fortea, and J. Moreno, "Cloud detection for CHRIS/Proba hyperspectral images," in *Proc. SPIE Remote Sens. Clouds Atmosphere X*, K. Schafer and A. Comeron, Eds., Bellingham, WA, 2006, vol. 5979, p. 597 91Q.
[36] L. Gomez-Chova, G. Camps-Valls, J. Amoros-Lopez, L. Guanter, L. Alonso, J. Calpe, and J. Moreno, "New cloud detection algorithm for multispectral and hyperspectral images: Application to ENVISAT/MERIS and PROBA/CHRIS sensors," in *Proc. IGARSS*, Denver, CO, Jul. 2006, pp. 2757–2760.
[37] G. Thuillier, M. Hers, P. Simon, D. Labs, H. Mandel, D. Gillotay, and T. Foujols, "Observation of the visible solar spectral irradiance between 350 and 850 nm during the ATLAS I mission by the SOLSPEC spectrometer," *Sol. Phys.*, vol. 177, pp. 41–61, 1998.
[38] R. M. Chapman, "Cloud distributions and altitude profiles from satellite," *Planet. Space Sci.*, vol. 9, no. 1/2, pp. 70–71, 1962.
[39] R. Preusker, A. Huenerbein, and J. Fischer, "Cloud detection with MERIS using oxygen absorption measurements," *Geophys. Res. Abstracts*, vol. 8, p. 09956, 2006.
[40] A. Berk, L. S. Bernstein, G. P. Anderson, P. K. Acharya, D. C. Robertson, J. H. Chetwynd, and S. M. Adler-Golden, "MODTRAN cloud and multiple scattering upgrades with application to AVIRIS," *Remote Sens. Environ.*, vol. 65, no. 3, pp. 367–375, Sep. 1998.
[41] S. Delwart, R. Preusker, L. Bourg, R. Santer, D. Ramon, and J. Fischer, "MERIS in-flight spectral calibration," *Int. J. Remote Sens.*, vol. 28, no. 3/4, pp. 479–496, Jan. 2007.
[42] F. Ranera, S. Plummer, and O. Arino, "A pragmatic solution for cloud detection and removal in MERIS L1B data," in *Proc. MERIS (A)ATSR Workshop*, Dec. 2005, p. 54.1.
[43] R. Duda and P. Hart, *Pattern Classification and Scene Analysis*. New York: Wiley, 1973.
[44] C. Brockmann, U. Krämer, K. Stelzer, V. Fournier-Sicre, J. Huot, S. Bélanger, F. Fell, G. Moore, P. Albert, B. Pinty, D. Antoine, D. Ramon, R. Doerffer, and F. Zagolsky, "Verification of the MERIS level 2 products," in *Proc. Envisat Validation Workshop*, Dec. 2002.
[45] J. Bezdek, W. Li, Y. Attikiouzel, and M. Windham, "A geometric approach to cluster validity for normal mixtures," *Soft Comput.—Fusion Foundations, Methodologies Applications*, vol. 1, no. 4, pp. 166–179, Dec. 1997.
[46] D. Davies and D. Bouldin, "A cluster separation measure," *IEEE Trans. Pattern Anal. Mach. Intell.*, vol. PAMI-1, no. 2, pp. 224–227, Apr. 1979.
[47] J. Rissanen, "Stochastic complexity and modeling," *Ann. Stat.*, vol. 14, no. 3, pp. 1080–1100, Sep. 1986.
[48] C. Chang, *Hyperspectral Imaging: Techniques for Spectral Detection and Classification*. Norwell, MA: Kluwer, 2003.
[49] A. Plaza and C.-I Chang, "Impact of initialization on design of endmember extraction algorithms," *IEEE Trans. Geosci. Remote Sens.*, vol. 44, no. 11, pp. 3397–3407, Nov. 2006.
[50] H. Ren and C.-I Chang, "Automatic spectral target recognition in hyperspectral imagery," *IEEE Trans. Aerosp. Electron. Syst.*, vol. 39, no. 4, pp. 1232–1249, Oct. 2003.
[51] R. Congalton and K. Green, *Assessing the Accuracy of Remotely Sensed Data: Principles and Practices*, 1st ed. Boca Raton, FL: CRC 1999.

Luis Gómez-Chova received the B.Sc. degree (with first class honors) in electronics engineering and the M.Sc. degree in electronics engineering in 2002 from the University of Valencia, Valencia, Spain, where he is currently working toward the Ph.D. degree.

Since 2000, he has been with the Electronics Engineering Department, University of Valencia, first enjoying a research scholarship from the Spanish Ministry of Education and, currently, as a Lecturer. His work is mainly related with pattern recognition and machine learning applied to remote-sensing multispectral images.

Mr. Gómez-Chova was the recipient of the National Award for Electronic Engineering from the Spanish Ministry of Education.

Gustavo Camps-Valls (M'04–SM'07) was born in Valencia, Spain, in 1972. He received the B.Sc. degree in physics, the B.Sc. degree in electronics engineering, and the Ph.D. degree in physics from the University of Valencia, Valencia, Spain, in 1996, 1998, and 2002, respectively.

He is currently an Associate Professor with the Electronics Engineering Department, University of Valencia, where he teaches electronics, advanced time-series processing, and signal processing. His research interests include neural networks and kernel methods for signal and image processing. He is the author (or coauthor) of 40 journal papers, more than 60 international conference papers, and several books and is the editor of the book *Kernel Methods in Bioengineering, Signal and Image Processing* (IGI, 2007). He is a Referee of many international journals.

Dr. Camps-Valls is currently serving on the Program Committees of the International Society for Optical Engineers, Europe, International Geoscience and Remote Sensing Symposium, and International Conference on Image Processing.

Javier Calpe-Maravilla (M'90) received the B.Sc. and Ph.D. degrees in physics from the University of Valencia, Valencia, Spain, in 1989 and 1993, respectively.

He is currently an Assistant Professor with the Electronics Engineering Department, University of Valencia. He is the holder of an industrial patent and has coauthored more than 70 papers in scientific magazines and 150 communications to conferences. He has led 28 projects with private companies and 18 with public funds, including coleading one funded by the EU (SmartSpectra). His research activities include remote sensing, digital signal processing, and its industrial applications.

Luis Guanter received the B.Sc. degree (with first class honors) in physics and the M.Sc. and Ph.D. degrees in environmental physics and thermodynamics from the University of Valencia, Valencia, Spain, in 2002, 2004, and 2007, respectively.

He is currently with the GeoForschungsZentrum-Potsdam, Potsdam, Germany. His research interests include atmospheric correction of satellite and airborne data, retrieval of atmospheric components, atmospheric radiative transfer modeling, and sensor calibration.

José Moreno (A'89) received the B.Sc. and Ph.D. degrees in physics from the University of Valencia, Valencia, Spain, in 1986 and 1992, respectively.

He was a Principal Investigator for the Environmental Satellite (ENVISAT) and Compact High Resolution Imaging Spectrometer-Project for On-Board Autonomy (CHRIS-PROBA) Projects. He is currently a Professor of earth physics with the Department of Earth Sciences and Thermodynamics, University of Valencia. He has been involved in many international projects and research networks, where he was responsible for studies and campaigns related to the preparation of several future satellite missions. He is the author of many publications in the field, including several book chapters. His main research interests are the modeling and monitoring of land surface processes.

Dr. Moreno was an Associate Editor for the IEEE TRANSACTIONS ON GEOSCIENCE AND REMOTE SENSING from 1994 to 2000. He was a member of the Earth Sciences Advisory Committee, European Space Agency, from 1998 to 2002, Space Station Users Panel, and other international advisory committees.

IEEE TRANSACTIONS ON

GEOSCIENCE AND REMOTE SENSING

A PUBLICATION OF THE IEEE GEOSCIENCE AND REMOTE SENSING SOCIETY

DECEMBER 2007 VOLUME 45 NUMBER 12 IGRSD2 (ISSN 0196-2892)

PART II OF TWO PARTS

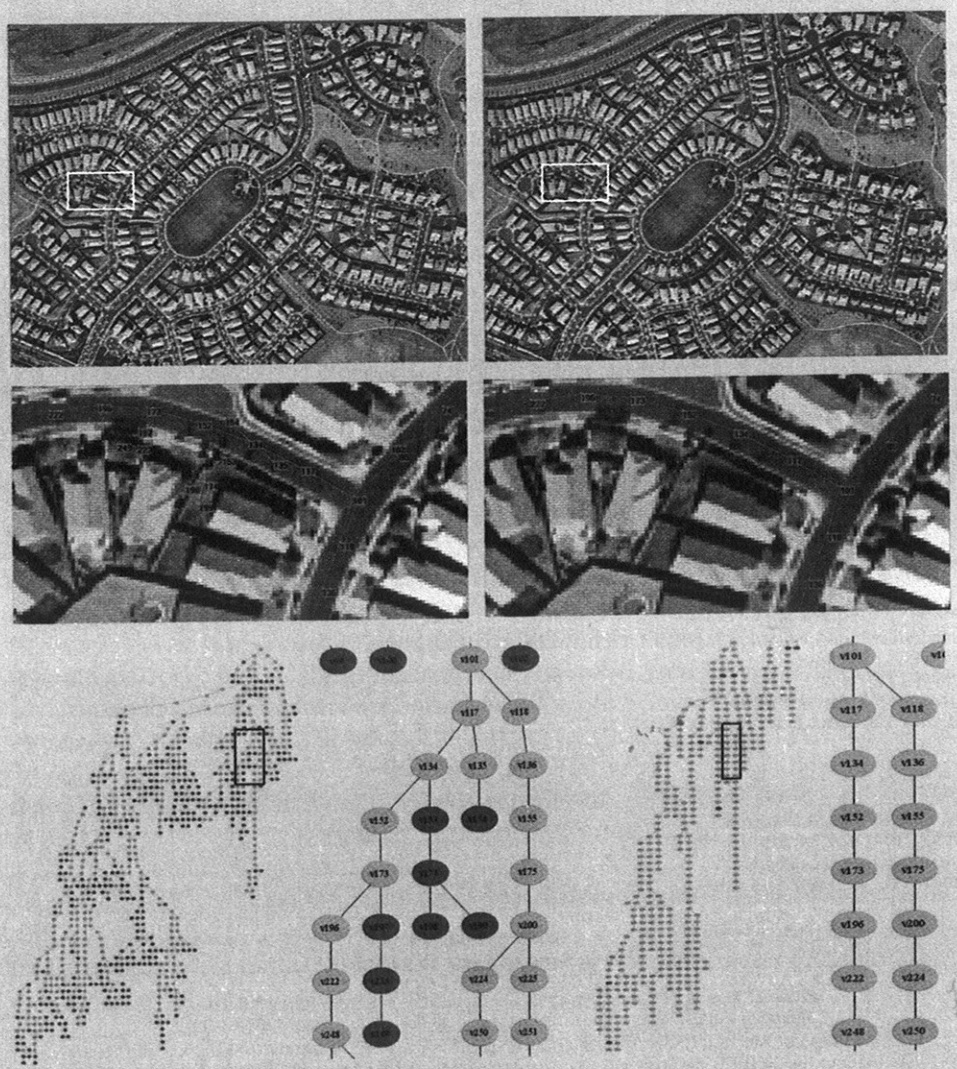

A new two-step approach for automated extraction of road networks from aerial images. In most cases the road tracker suffers from oversegmentation and leakage (top left), which must be postprocessed (top right). (Middle) Zoomed-in views. (Bottom middle) Zoomed-in view of a portion of the road tree in the bottom left. (Bottom right) Pruned tree using our method.

IEEE

IEEE TRANSACTIONS ON

GEOSCIENCE AND REMOTE SENSING

A PUBLICATION OF THE IEEE GEOSCIENCE AND REMOTE SENSING SOCIETY

DECEMBER 2007 VOLUME 45 NUMBER 12 IGRSD2 (ISSN 0196-2892)

PART II OF TWO PARTS

REGULAR ISSUE PAPERS

CORRESPONDENCE

(Contents Continued on Page 4018)

IEEE

ISI Web of Knowledge℠

Journal Citation Reports®

WELCOME | HELP | RETURN TO LIST

2007 JCR Science Edition

Journal: IEEE TRANSACTIONS ON GEOSCIENCE AND REMOTE SENSING

Mark	Journal Title	ISSN	Total Cites	Impact Factor	Immediacy Index	Articles	Cited Half-life	Citing Half-life
☐	IEEE T GEOSCI REMOTE	0196-2892	9167	2.344	0.283	375	6.8	7.5

Cited Journal | Citing Journal | Source Data

CITED JOURNAL DATA | CITING JOURNAL DATA | IMPACT FACTOR TREND | RELATED JOURNALS

Journal Information

Full Journal Title: IEEE TRANSACTIONS ON GEOSCIENCE AND REMOTE SENSING
ISO Abbrev. Title: IEEE Trans. Geosci. Remote Sensing
JCR Abbrev. Title: IEEE T GEOSCI REMOTE
ISSN: 0196-2892
Issues/Year: 12
Language: ENGLISH
Journal Country/Territory: UNITED STATES
Publisher: IEEE-INST ELECTRICAL ELECTRONICS ENGINEERS INC
Publisher Address: 445 HOES LANE, PISCATAWAY, NJ 08855
Subject Categories: GEOCHEMISTRY & GEOPHYSICS SCOPE NOTE | VIEW JOURNAL SUMMARY LIST | VIEW CATEGORY DATA

ENGINEERING, ELECTRICAL & ELECTRONIC SCOPE NOTE | VIEW JOURNAL SUMMARY LIST | VIEW CATEGORY DATA

REMOTE SENSING SCOPE NOTE | VIEW JOURNAL SUMMARY LIST | VIEW CATEGORY DATA

Journal Impact Factor

Cites in 2007 to articles published in: 2006 = 759
2005 = 725
Sum: 1484

Number of articles published in: 2006 = 343
2005 = 290
Sum: 633

Calculation: Cites to recent articles / Number of recent articles = 1484 / 633 = **2.344**

Journal Immediacy Index

Cites in 2007 to articles published in 2007 = 106
Number of articles published in 2007 = 375